ELSEVIER

Contents lists available at ScienceDirect

# Journal of Magnetic Resonance

journal homepage: www.elsevier.com/locate/jmr



# Single-shot spatially-localized NQR using field-dependent relaxation rates



Cheng Chen<sup>a,\*</sup>, Xinyao Tang<sup>a</sup>, Naren Vikram Raj Masna<sup>b</sup>, Swarup Bhunia<sup>b</sup>, Soumyajit Mandal<sup>a</sup>

#### ARTICLE INFO

Article history:
Received 15 July 2019
Revised 22 November 2019
Accepted 22 November 2019
Available online 12 December 2019

Keywords: NQR imaging Zeeman splitting Laplace inversion Classification Authentication

#### ABSTRACT

Nuclear quadrupole resonance (NQR) is commonly used to characterize solid materials containing quadrupolar nuclei. For example, NQR is a promising technique for detecting plastic explosives and other forbidden substances as well as for authenticating pharmaceutical products. Spatially-resolved NQR measurements are of particular interest for enabling automated sample positioning, evaluation of sample heterogeneity, and chemometric authentication of objects. This paper proposes a rapid "single-shot" method for spatially-resolved NQR with the potential to benefit such applications. The proposed method takes advantage of the fact that certain NQR relaxation rates are field-dependent: the observed field dependence is used to convert relaxation time distributions measured in a static field gradient (estimated via Laplace inversion of time-domain data) into spatial distributions. The method was validated using <sup>35</sup>Cl and <sup>37</sup>Cl NQR of sodium chlorate and other compounds. Effective spatial resolution was also improved by using machine learning (ML) to classify the measured spatial distributions. In particular, experimental results demonstrate accurate ML-based classification of 3D-printed objects containing arbitrary binary distributions of sodium chlorate. Such distributions can thus be used as NQR-based "embedded barcodes" for authenticating high-value objects.

© 2019 Elsevier Inc. All rights reserved.

#### 1. Introduction

NQR is a non-destructive, non-contact, and chemically-specific spectroscopic method that requires no sample preparation, which makes it an ideal candidate for distinguishing between different chemical species and even polymorphic forms of the same species [1,2]. In particular, NQR has attracted a lot of attention for detecting (i) illicit substances such as bulk narcotics, and (ii) explosives within buried landmines and baggage [3,4]. Moreover, it is a quantitative technique: the magnitude of received NQR signals can be directly converted to the number of quadrupolar nuclei of a particular isotope that are present within the sample. As a result, NQR is also emerging as a powerful method for authentication of pharmaceutical products [5,6].

Despite the advantages discussed above, there are practical difficulties in applying NQR to field applications, i.e., outside of laboratory environments. For example, NQR spectra of common nuclei such as <sup>14</sup>N and <sup>35</sup>Cl suffer from inherently low sensitivity, so rel-

E-mail addresses: cxc717@case.edu (C. Chen), xxt81@case.edu (X. Tang), nmasna@ufl.edu (N.V.R. Masna), swarup@ece.ufl.edu (S. Bhunia), sxm833@case.edu (S. Mandal).

atively large sample volumes (typically, several grams) are required to obtain sufficient signal-to-noise ratio (SNR) at room temperature. The signal is also easily corrupted by external radio frequency (RF) interference. In addition, it is important to note that NQR cannot be used for analyzing liquids, for which the signal is averaged out due to random molecular motion. Various approaches have proposed to address the specific issues of low sensitivity and external interference. These include improvements to the RF pulse sequences [7], hardware designs [8], and signal processing algorithms [9], as well as several cross polarization techniques [10,11].

Solid-state NMR imaging plays an important role in biomedical engineering and material science. In particular, it is a valuable tool for studying the local dynamics, kinetics, and thermodynamics of a variety of complex samples. However, it is generally only applied to spin-1/2 nuclei such as <sup>1</sup>H and <sup>13</sup>C. Spatially-resolved NQR (i.e., NQR imaging) would greatly expand the applications of magnetic resonance imaging (MRI) by enabling the characterization of solid materials containing quadrupolar nuclei. One potential application is to obtain information on the heterogeneity of blister packs containing multiple dose units (pills or capsules), particularly ones placed within sealed packets or bottles that are opaque

<sup>&</sup>lt;sup>a</sup> Case Western Reserve University, 10900 Euclid Ave, Cleveland, OH 44106, USA

<sup>&</sup>lt;sup>b</sup> University of Florida, Gainesville, FL 32611, USA

<sup>\*</sup> Corresponding author.

to optical scanners. Dose units in a single pack may have different active pharmaceutical ingredients (APIs) and impurities, and the presence of placebo dose units may generate false negative screening results from volumetric measurements [12]. Moreover, previous research has shown that the spatial position and distribution of such pills or capsules can result in significant changes in detected NQR signal amplitude [13]. Thus, spatially-resolved NQR measurements are important for obtaining quantitative results from both homogeneous and heterogeneous samples.

Standard NMR-based imaging approaches cannot be directly applied to NQR, since there is excessive line broadening due to the spatially-varying Zeeman splitting caused by magnetic field gradients. Alternatively, Matsui et al. proposed to utilize the Zeeman-perturbed NOR power pattern. The width of the pattern is proportional to the Zeeman field applied across the test object if the zero-field NOR line is sufficiently narrow. Therefore, a onedimensional (1D) spatial spin density distribution can be obtained by measuring spectra at different zero-field points in the sample [14]. Another NQR imaging technique is based on a rotating frame method. In this " $\rho$ NQRI" approach, the spatial information is encoded using gradients in the RF amplitude of the excitation pulse. The projection of spin density of the sample along the gradient direction can then be reconstructed by applying a deconvolution algorithm [15]. There is no static magnetic field applied, therefore no Zeeman splitting effects have to be taken into account. However, relatively short RF pulses have to be applied, which places design constraints on the peak transmit power level, receiver recovery time, and other parameters of the front-end electronics [16]. Also note that NQR imaging research has generally been limited to 35Cl due to its relatively high resonant frequency (and thus high sensitivity), with  $\rho$ NQRI of <sup>14</sup>N being proposed only

The idea of using NQR spectra to provide a chemical "fingerprint" unique to a product's active ingredients has been developed over the years [18-20]. Adding spatial information effectively adds another dimension to such bulk fingerprints, which significantly improves their uniqueness and unclonability. It is possible to use available imaging techniques such as rotating-frame NOR to obtain such spatial information. However, current methods are timeconsuming and instrumentation-unfriendly. Thus, there is a need to develop spatially-resolved NQR measurement techniques that are (i) rapid, and (ii) simple to implement. In this paper, we propose a simple but novel approach to spatially-localized NQR that relies on field-dependent relaxation rates. We observe that the relaxation rate  $T_{2_{eff}}$  of certain compounds increases monotonically with Zeeman splitting, and thus with the magnitude of a static field  $(B_0)$  applied to the sample. Therefore, field-dependent 1D localization information can be encoded into relaxation rates. The theoretical feasibility of the approach is discussed in detail. In addition to the basic NQR setup, the proposed method also requires a static  $B_0$ gradient. However, the resulting experimental setup is still simple and does not place any additional constraints on the front-end electronics. Moreover, the whole experiment can be completed in a single scan once calibration has been performed. This "singleshot" advantage can significantly accelerate NQR imaging compared to earlier methods, thus making it suitable for (i) rapidly detecting sample position within the detector, and (ii) characterizing the heterogeneity of pharmaceutical samples. Furthermore, we demonstrate that the effective spatial resolution of the proposed approach can be improved by combining it with machine learning (ML)-based classification techniques. Finally, we demonstrate that the classification results can be used to decode 1D binary patterns that function as "embedded NQR barcodes". This working example demonstrates the feasibility of our approach in practical applications.

#### 2. Theory

#### 2.1. Resonant frequencies

NQR spectra are generated by resonant transitions between nuclear energy levels of an atomic ground state. The energy levels are created by interactions between nuclear quadrupolar moments and local electric field gradients (EFGs). The nuclear Hamiltonian relevant for zero-field NQR is given by

$$H_{Q} = \frac{\omega_{Q}}{3} \left[ 3I_{z}^{2} - I(I+1) + \frac{\eta}{2} \left( I_{+}^{2} + I_{-}^{2} \right) \right], \tag{1}$$

where  $\omega_{\mathbb{Q}}$  is the quadrupolar coupling constant,  $\eta$  is the asymmetry parameter of the EFG tensor in the principal axis system fixed on the nucleus, and  $I_z$ ,  $I_+$ , and  $I_-$  are spin operators. In particular, there are two doubly-degenerate levels for nuclei with I=3/2 (such as  $^{35}$ Cl and  $^{37}$ Cl), which are given by

$$E_{\pm 3/2} = \frac{1}{4} \omega_{Q} \sqrt{1 + \frac{\eta^{2}}{3}}, E_{\pm 1/2} = -\frac{1}{4} \omega_{Q} \sqrt{1 + \frac{\eta^{2}}{3}}. \tag{2}$$

Thus, there is only one (non-zero) transition frequency

$$\omega_{\alpha\beta} = \frac{\omega_Q}{2} \sqrt{1 + \frac{\eta^2}{3}}. (3)$$

Note that the presence of only one transition (i.e., resonance) frequency means that one cannot determine both  $\omega_{\mathbb{Q}}$  and  $\eta$  within one NQR measurement. The most common solution is to apply a small magnetic field to break the degeneracy, thus resulting in four resonance frequencies. In this case, the strength of each transition is a function of the relative orientations of the static magnetic field, RF magnetic field, and local EFGs, thus allowing  $\eta$  to be calculated accordingly [21]. The energy levels with and without a magnetic field are qualitatively shown in Fig. 1.

# 2.2. Pulse sequences

By default, we utilize (i) single spin echoes, and (ii) the classical spin-lock spin-echo (SLSE) pulse sequence for data collection. The SLSE sequence consists of an initial excitation pulse and a long train of refocusing pulses separated by the echo period  $t_E$ , as shown in Fig. 2.

# 2.3. Effects of Zeeman splitting

Zeeman-perturbed NQR (ZP-NQR) was first observed by Hahn and Herzog. In [22], they reported that the relaxation time constant T<sub>2,eff</sub> of <sup>35</sup>Cl spin echoes in single-crystal sodium chlorate (NaClO<sub>3</sub>) is a function of the magnitude and direction of an external static magnetic field  $B_0$ , i.e., is modified by the Zeeman splitting. Here T<sub>2.eff</sub> is determined by the dynamic components of relaxation processes, as opposed to the static components that determine the relaxation time constant  $T_2^*$  for free-induction decays and individual echo envelopes (see Fig. 2). Thus,  $T_{2.eff}$  excludes the effects of spin-lattice coupling (i.e.,  $T_1$  relaxation) but includes due to (i) time-varying EFGs and external fields, and (ii) spin-spin coupling. Interestingly, the value of  $T_{2,eff}$  was found to increase with the magnitude of the applied field  $B_0$  and approach a constant at large field strengths. On the other hand,  $T_2^*$  (which is generally much smaller than  $T_{2,eff}$ ) is dominated by dephasing due to static inhomogeneities in both the EFG and the  $B_0$  field across the sample that is removed (i.e., refocused) at the peak of each spin echo. Unlike for  $T_{2,eff}$ , the value of  $T_2^*$  tends to decrease with  $B_0$  since the field seen by the nuclei becomes more inhomogeneous [23].

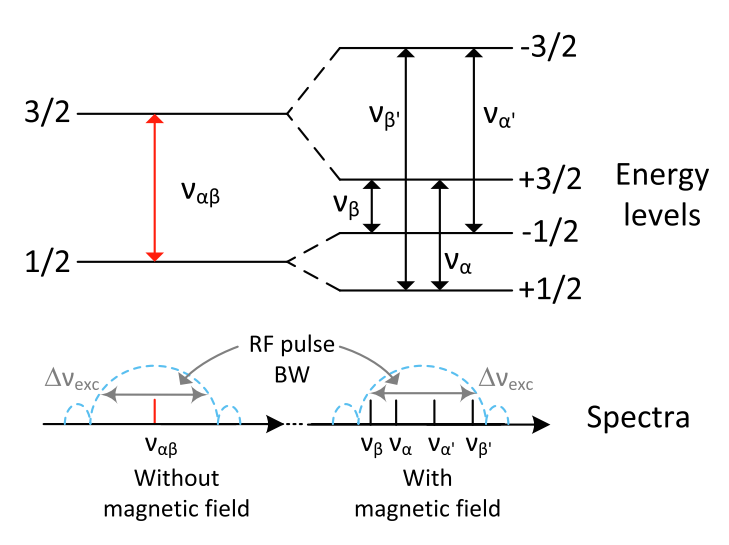
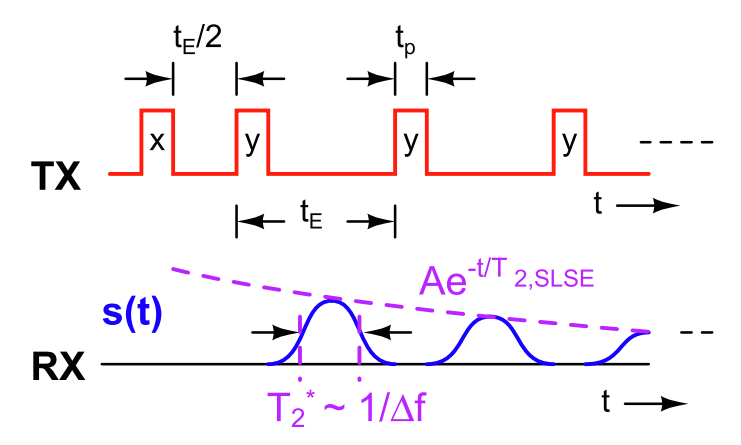
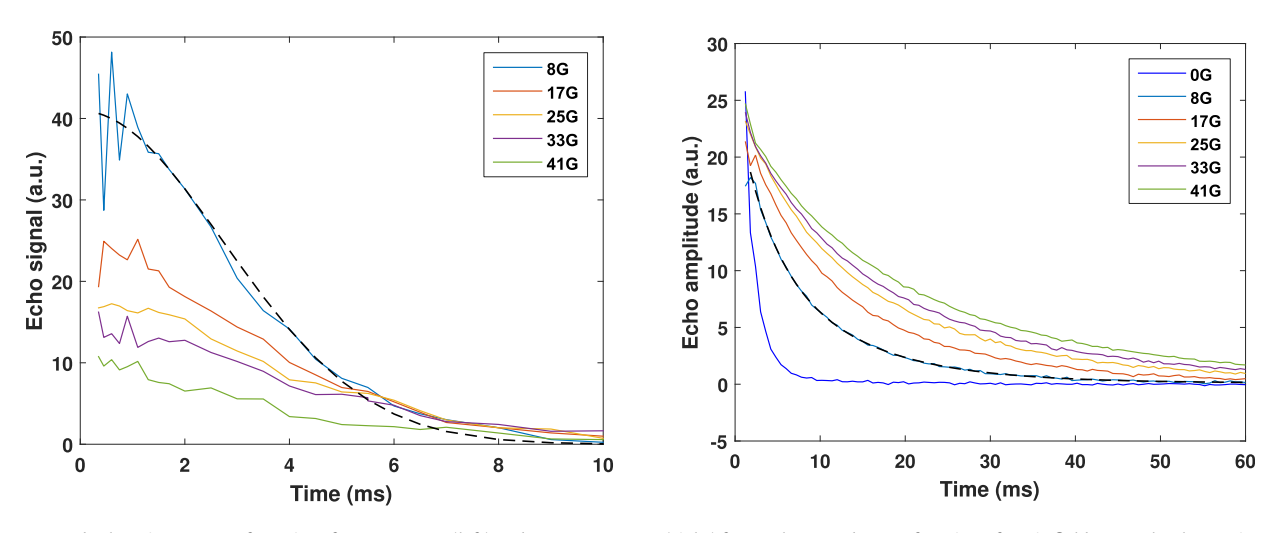


Fig. 1. Energy levels of an I = 3/2 nucleus subject to a strong quadrupolar interaction and a weak magnetic field. The energy level splitting due to the magnetic field is greatly exaggerated. The lower row shows (i) the resulting spectral lines, and (ii) the spectrum of a typical RF excitation pulse used to measure them.



**Fig. 2.** Basic spin-locked spin echo (SLSE) pulse sequence used for pulsed NQR experiments, and the resulting received signal s(t). Here A is the initial signal amplitude,  $T_{2,\text{SLSE}}$  is the decay time constant,  $T_2^*$  is the echo width, and  $\Delta f \sim 1/T_2^*$  is the measured NQR line width.



**Fig. 3.** Measured relaxation curves of a series of SE sequences (left) and a SLSE sequence (right) for NaClO<sub>3</sub> powder as a function of static field strength when  $B_0$  is parallel to  $B_1$ . The data was measured at 20 °C. The pulse length was 50 μs in both cases for a nominal flip angle of 120° (which corresponds to  $B_1 = 16.0$  G), while  $t_E = 600$  μs for the SLSE sequence. Note that the first two points were removed from the SLSE sequence data in order to obtain a better fit.

The NQR signal for a crystalline powder is related to that for a single crystal by a powder average, i.e., an integral over all possible random orientations of the EFG tensor with respect to the RF coil axis [24]. As an example, we studied the field-dependent relaxation of NaClO<sub>3</sub> powder. Fig. 3 shows decay curves obtained at different magnetic fields  $B_0$  using (i) a series of spin echo (SE) experiments with different delay times, and (ii) a SLSE pulse sequence. In both cases,  $B_0$  was kept parallel to the RF field  $B_1$ applied to the sample, and the amplitude of  $B_1$  was kept fixed at ~16.0 G. An decrease in relaxation rate with increasing magnetic field is observed for both pulse sequences. For convenience, we continue to denote the corresponding time constant by  $T_{2.eff}$  when the discussion is applicable to both SE and SLSE sequences. However, when referring specifically to either sequence, we replace  $T_{2,eff}$  with  $T_{2,SE}$  or  $T_{2,SLSE}$ , respectively, to avoid confusion. In particular, Fig. 3 shows that (i) the SE relaxation curves are well-fit by

Gaussian functions  $s(t)=s(0)\exp\left(-\frac{t^2}{2T_{2,SE}^2}\right)$ ; and (ii) the SLSE relaxation curves are well-fit by mono-exponentials  $s(t)=s(0)\exp\left(-t/T_{2,SLSE}\right)$ . As an example, the dashed lines in the figure show best-fitting decay curves for both sequences when  $B_0=8$  G. These results are in general agreement with earlier work [23,25]. They suggest that SE relaxation is dominated by spin-spin dipole coupling, some of which is refocused by the SLSE sequence (thus explaining why  $T_{2,SLSE}>T_{2,SE}$ ).

Next, we would like to compare  $T_{2.eff}$  with  $T_2^*$  for both sequences; note that  $T_2^*$  is inversely proportional to the frequency-domain line width of the received echoes. However, simply adding up the received echoes in Fig. 3 to maximize SNR prior to estimating  $T_2^*$  results in  $T_{2.eff}$ -weighting of the echo amplitudes, which should be removed for clarity. For example, the sum of the received echoes from a SLSE sequence can be represented as

$$S_{tot} = S(0) \left( \frac{T_{2,SLSE}}{t_E} \right) \left( 1 - e^{-N_E t_E / T_{2,SLSE}} \right),$$
 (4)

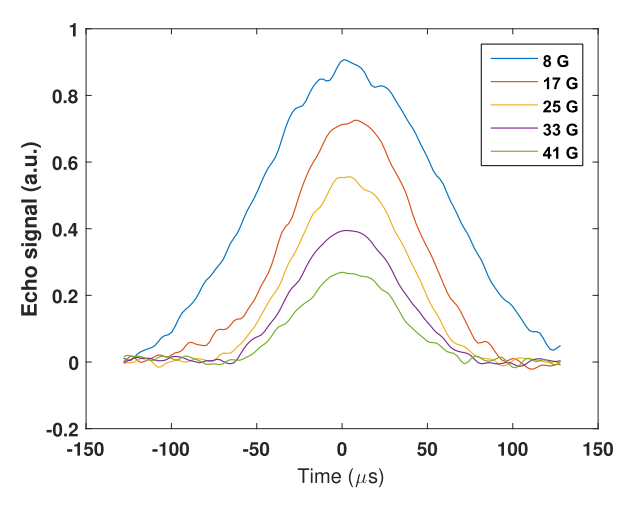
where  $N_E$  is the total number of echoes. A detailed derivation of Eqn. (4) is available in A. When enough echoes are acquired such that  $N_E t_E \gg T_{2,SLSE}$ , the equation simplifies to  $s_{tot} \approx s(0)(T_{2,SLSE}/t_E)$ . To remove the dependence on  $T_{2,SLSE}$ , we therefore plot  $s(0) \approx s_{tot}(t_E/T_{2,SLSE})$ . A similar process can be used to remove  $T_{2,SE}$  weighting from the SE data.

Fig. 4 shows the echo sums for the SE and SLSE sequences measured at different magnetic fields;  $T_{2,eff}$ -weighting has been removed for clarity. Table 1 summarizes the best-fitting values of  $T_{2,eff}$  and  $T_2^*$  for both sequences assuming Gaussian echo shapes.

For the SE sequence, a wide acquisition window is required to measure the broad echoes generated at zero magnetic field. As a result, the measured data after phase cycling still contains a significant amount of ring-down from the coil, preventing us from accurately calculating the relaxation times and echo integrals in this case. Thus, zero-field data from the SE sequence is not shown in the table. Also note that (i)  $B_0$  was kept parallel to  $B_1$ , and (ii) the specified values of  $B_0$  do not include the small Earth's field of 0.53  $\sim$ 0.53 G that was also present during the experiments.

It is interesting to observe from Table 1 that (i) for both sequences,  $T_2^*$  decreases with  $B_0$ , while  $T_{2,eff}$  increases; and (ii) both these trends are significantly more pronounced for the SLSE sequence. The fact that  $T_2^*$  decreases with  $B_0$  implies that the spectral linewidth  $\Delta f$  (which is approximately proportional to  $1/T_2^*$ ) is broadened by Zeeman splitting and  $B_0$  inhomogeneity, as expected. In particular, the spectral width of a Zeeman-perturbed NQR powder pattern is known to be proportional to  $B_0$  if the zero-field line is sufficiently narrow [14]. On the other hand, the fact that  $T_{2,eff}$  shows the reverse trend, i.e., increases with  $B_0$ , requires more explanation. While a similar effect was seen by Hahn and Herzog for the SE sequence using single-crystal NaClO<sub>3</sub> [22], as far as we know it has not been well-studied either for powder samples, or for the SLSE sequence.

The observed behavior of  $T_{2,eff}$  relaxation in weak magnetic fields can be qualitatively explained using a model which assumes that the local magnetic field at a CI site is due primarily to the dipolar field of the neighboring nuclei. We assume that field-dependent  $T_{2.eff}$  relaxation arises from homonuclear coupling (Cl-Cl) rather than heteronuclear coupling (Na-Cl), since Zeeman splitting of the Na and Cl resonances should have little effect on the latter. For  $B_0 = 0$ , the coupled pair of Cl spins are in one of two degenerate energy levels ( $\pm 3/2$  and  $\pm 1/2$ ), and the resulting relaxation diagram is analogous to that for dipolar coupling in spin-1/2 NMR, as shown in Fig. 5. The transition rates in this diagram are given by the well-known expressions for dipolar coupling between identical ("like") spins [26]. Once a non-zero  $B_0$  field is applied, the single NQR line splits into a quadruplet (see Fig. 1), which is subsequently further broadened by powder averaging. To first order, this process can be modeled by assuming that the Cl spins are divided into four non-equivalent groups. There are  $4^2 = 16$  possible states for pair of spins belonging to these groups, of which only 4 behave as "like" spins. As a result, most of the resulting transition rates are given by those for non-equivalent ("unlike") pairs of spins. Since transverse cross-relaxation is present for "like" but not "unlike" pairs of spins [27], the net result for both SE and



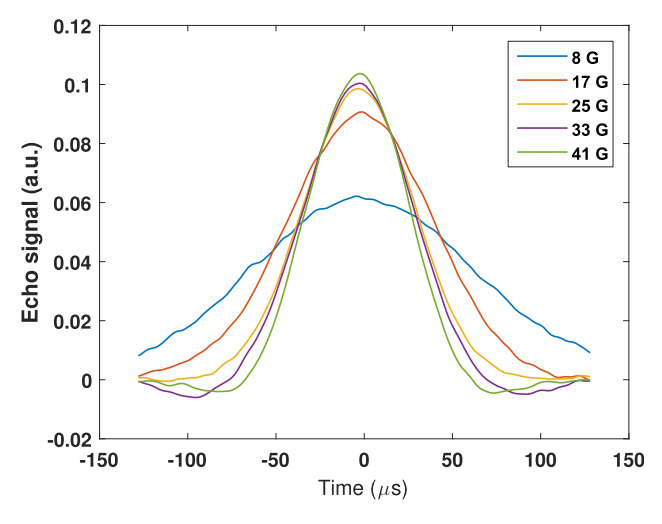
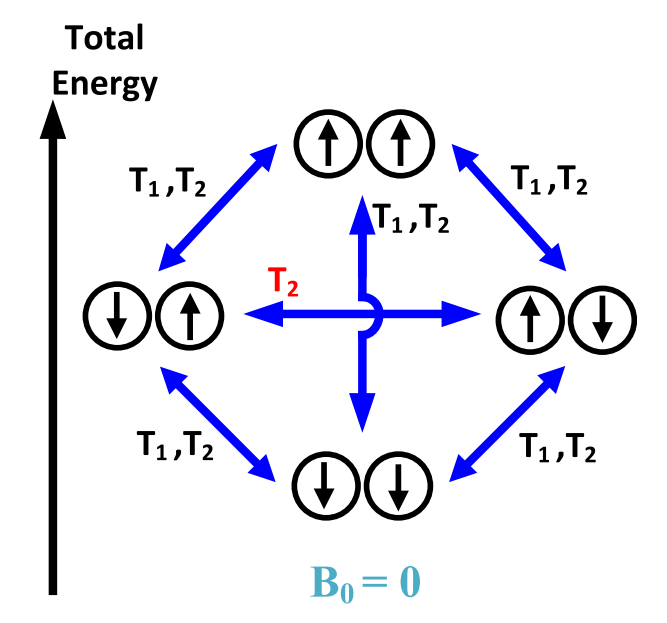


Fig. 4. Non-T<sub>2.eff</sub> weighted echo sums for the SE (left) and SLSE (right) pulse sequences for the same data shown in Fig. 3.

**Table 1** Best-fitting values of  $T_2^*$  and  $T_{2,eff}$  for SE and SLSE pulse sequences at different  $B_0$  fields.

Magnetic field (G)	0	8	16.8	25	33	41
SE $T_2^*$ (µs)	N/A	122.1	85.0	75.4	70.5	65.4
SE decay time constant $T_{2.SE}$ (ms)	N/A	3.9	4.6	5.2	5.5	5.1
SE echo integral (a.u.)	N/A	113.31	65.11	42.77	29.19	19.19
SLSE $T_2^*$ ( $\mu$ s)	373	164	116	90	76	68
SLSE decay time constant $T_{2,SLSE}$ (ms) @ $t_E=600~\mu$ s	1.4	12.0	17.0	21.3	24.9	28.0
SLSE echo integral (a.u.)	N/A	9.38	9.23	7.69	6.92	6.48



**Fig. 5.** Relaxation due to dipole-dipole coupling between pairs of NQR spins (I=3/2) in two degenerate states (represented by up and down arrows, respectively) at  $B_0=0$ . Note that spins are not restricted to these eigenstates, but can also form superpositions. However, we only show the former for simplicity.

SLSE sequences is a decrease in the transverse relaxation rate (i.e., an increase in  $T_{2.eff}$ ) as  $B_0$  increases.

It is worth noting that the observed SLSE echo decays are also dependent on (i) the value of  $t_E$ , and (ii) the magnitude of  $B_1$ . Firstly,  $T_{2,SLSE}$  decreases as  $t_E$  increases, as commonly observed for pulsed spin-locking sequences [25,28]. In order to study the second effect, we decreased the RF power level while increasing the SLSE pulse length  $t_p$  to keep the nominal flip angle constant (data not shown for conciseness). We found that  $T_{2,SLSE}$  goes up slightly as  $B_1$  decreases, while the initial signal amplitude decreases. Both results are related to the decrease in RF pulse bandwidth (and thus refocusing bandwidth) as  $B_1$  decreases.

For the SE sequence, it is also possible to estimate the relationship between echo amplitude  $s(t_E)$  and static magnetic field  $B_0$  for powder samples; here  $t_E/2$  is the time delay between the excitation and refocusing pulses and  $t_E$  is again the echo period. The SE amplitude for single-crystal NaClO<sub>3</sub> (assuming  $\eta=0$  for simplicity) is given by  $s=s_++s_-$  [23], where

$$\begin{split} s(t_{E},\theta,\phi,B_{0})_{\pm} &= -2\sqrt{3}M_{0}(\cos\theta_{\pm})\sin(\sqrt{3}\omega_{1}t_{p}\cos\theta_{\pm}) \\ &\times \sin^{2}\left[(\sqrt{3}\omega_{1}t_{p}\cos\theta_{\pm})/2\right] \\ &\times \left(\left(\frac{\beta_{\pm}-1}{\beta_{\pm}}\right)^{2}\cos\left[\omega_{0}(\cos\theta_{\pm})(3+\beta_{\pm})(t-t_{E})/2\right] \\ &+ \left(\frac{\beta_{\pm}+1}{\beta_{\pm}}\right)^{2}\cos\left[\omega_{0}(\cos\theta_{\pm})(3-\beta_{\pm})(t-t_{E})/2\right] \right) \\ &\times \exp\left\{-\left[(t-t_{E})^{2}/2T_{2}^{*2} + t^{2}/T_{2,SE}^{2}(B_{0},\phi)\right]\right\}. \end{split}$$
 (5)

Here '+' and '-' refer to Cl nuclei assigned to the two groups which correspond to the two non-equivalent directions for Na-Cl axes (with respect to  $B_0$ ) that occur within the crystal [23]. Also  $M_0$  is a constant,  $\omega_0 = \gamma B_0$  and  $\omega_1 = \gamma B_1$  where  $\gamma$  is the gyromagnetic ratio,  $\phi$  is the angle between  $B_0$  and the < 100 > direction in NaClO<sub>3</sub>,  $\theta$  is the angle between  $B_0$  and the Na-Cl bond, and  $\beta_{\pm} = (1 + 4 \tan^2 \theta_{\pm})^{1/2}$ . As mentioned previously, to extend this result to powder samples, we need to numerically integrate Eqn. (5) over the angular dependence, i.e., over  $\theta$  and  $\phi$ . Note that two assumptions are necessary for this procedure to be valid: (i) the sample consists of a large number of single crystals which are oriented at random directions; and (ii) the external fields are homogeneous over the sample. In this case, the received echo can be found by assuming that all values of  $\theta$  and  $\phi$  occur with equal probability, which results in a weighted average over all orientations:

$$\langle s(t_E, B_0) \rangle = \frac{1}{4\pi} \int_0^{2\pi} \int_0^{\pi} s(t_E, \theta, \phi, B_0) \sin \theta d\theta d\phi.$$

Fig. 6 compares the estimated and measured echo amplitudes  $s(t_E)$  for NaClO<sub>3</sub> powder as a function of  $B_0$ ; all results have been normalized to those for  $B_0 = 0$ . The dependence versus  $B_0$  is generally similar in the two cases, and is also in agreement with that presented by Ramachandran et al. [29]. The small but noticeable differences between the theoretical and measured curves likely arise from the fact that the actual asymmetry parameter for the sample may not be zero as assumed in the analysis.

#### 2.4. Laplace inversion

Compared to SE, the SLSE sequence has the advantage of generating multiple echoes, thus allowing "single-shot" estimation of  $T_{2.SLSE}$ . Thus, we will focus on it for the remainder of the paper.

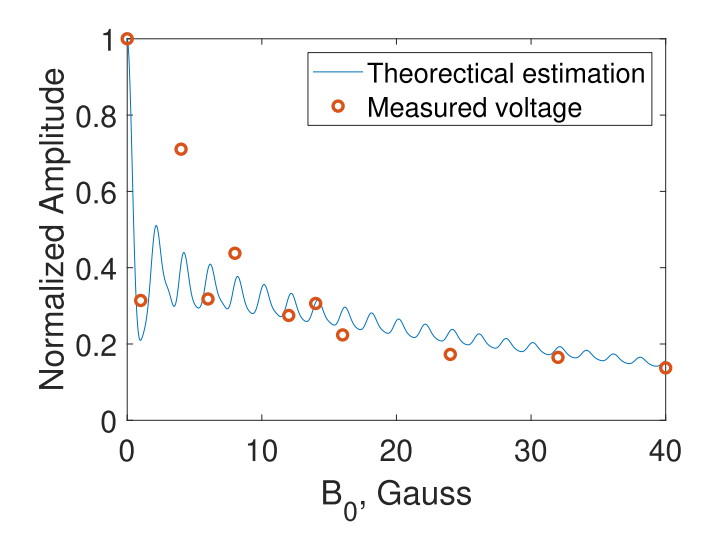


**Fig. 6.** Estimated and measured received SE amplitudes for NaClO<sub>3</sub> powder (after normalization) as a function of  $B_0$  for  $t_E = 2200 \,\mu s$ .

Given the averaged time-domain data s(t) from an SLSE sequence, we use a regularized inverse Laplace transform (ILT) algorithm to generate  $T_{2.SLSE}$  distribution functions  $f(T_{2.SLSE})$  [30]. The width of the distribution is determined by the need to use regularization to obtain a robust fit to the data. In particular, we minimize a function of the form

$$g(K,F) = \|M - KF\|^2 + \alpha \|F\|^2, \tag{7}$$

where M, K, and F represent the data matrix, measurement kernel (determined by the pulse sequence), and the  $T_{2,SLSE}$  distribution, respectively.

The first term in g(K,F) measures the mean-squared difference  $(l_2\text{-norm})$  between the data (M) and the fit to it (KF). The second term provides Tikhonov regularization, and its amplitude is controlled by the so-called regularization parameter  $\alpha$ . The effect of this regularization term is to favor solutions with a small  $l_2$ -norm  $\|F\|^2$ , i.e., generate distributions that are smooth and hence robust to noise in the data. As  $\alpha$  increases, the overall fitting error remains nearly constant before starting to sharply increase. Thus, an optimal value of  $\alpha$  should be chosen that keeps the fitting error close to its minimum value while at the same time resulting in relatively smooth distributions. Several algorithms can be used for this purpose; here we used the well-known Butler-Reeds-Dawson (BRD) method [31].

#### 2.5. Machine learning for chemical fingerprinting

Chemical fingerprinting or extrinsic tagging is widely applied in the fields of medicine and chemistry. Moreover, recent work on identification and quality control of food and pharmaceutical products relies heavily on the development of chemical fingerprint analysis. In particular, fingerprinting is a very effective method for detecting counterfeit medicines and adulterated dietary supplements, which are a growing threat all over the world [32]. NQR, as a volumetric measurement, shows excellent performance in characterizing solid samples. NQR spectra are thus highly suitable as chemical fingerprints for medicines and material authentication; a more detailed discussion is available in [6]. In particular, the use of embedded NQR-active "tags" for authenticating medicines and dietary supplements has been discussed in our earlier work [20]. Here we extend the concept of embedded NQR-active tags to spatially-varying binary tagging patterns ("NQR barcodes") that provide improved security.

One possible implementation is shown in Fig. 7. The applied detector is a movable solenoid that fits around the sample (i.e., a standard medicine bottle), thus generating a stronger and more uniform  $B_1$  field than small flat surface detectors and resulting in higher SNR. The operational procedure is based on (i) quickly extracting the digital data (e.g., NQR signal amplitude) stored within the sample at each detector position, (ii) combining data obtained at several positions to generate a multi-bit chemical barcode, and (iii) cross-referencing this result with other information (e.g., product information obtained from an optical barcode) for verification purposes. Machine learning algorithms running either locally (on the spectrometer) or on the cloud are well-suited for extracting digital barcode data by classifying measured NQR signals into categories.

# 3. Results

We use NaClO<sub>3</sub> as our main experimental sample, since it has (i) significant field-dependent relaxation (see Table 1), and (ii) well-studied pressure- and temperature-dependent NQR characteristics [33–36]. In particular, the observed field-dependent behavior of  $T_{2,SISE}$  at weak magnetic fields provides us with a straightforward

method to perform spatially-resolved experiments, i.e., NQR imaging. Our approach relies on encoding spatial information within the values of  $T_{2.SLSE}$  that result on applying a gradient magnetic field. An immediate application is to improve the spatial resolution of the "NQR barcode"-based authentication approach shown in Fig. 7. In particular, if we can obtain  $M_1 > 1$  bits of spatial information at each detector position with the proposed imaging technique, then we can combine it with data from  $M_2$  detector positions to realize a  $M_1M_2$ -bit barcode with greatly improved security.

#### 3.1. Basic setup and calibration

Fig. 8 shows the setup used for our imaging experiments. The probe (solenoid with 10 turns and a length of  $\sim$ 40 mm) and matching network are set up between a pair of large coils on the same axis. When the radius of these coils is equal to the distance between them, and they are connected such that their currents flow in the same direction, a uniform magnetic field  $B_0$  is generated within the probe. This "Helmholtz coil" configuration was used to measure the field-dependent relaxation behavior for NaClO<sub>3</sub> summarized in Table 1. The strength of the uniform magnetic field can be estimated as

$$B_0 = \left(\frac{4}{5}\right)^{\frac{3}{2}} \frac{\mu_0 NI}{R},\tag{8}$$

where  $\mu_0$  is the permeability, N is the number of turns, I is the coil current and R is the coil radius. Fig. 9(a) compares the theoretical  $B_0$  field generated by the Helmholtz coils with its measured value at the center of the sample volume.

Furthermore, as mentioned in Section 2.3, after averaging over all orientations of the principal axes, the only part of  $B_0$  which will remain important in determining  $T_{2.SLSE}$  is its magnitude  $|B_0|$ . As a result, we cannot simply reverse the Helmholtz coils to create a symmetric gradient field with respect to the middle point between them (assumed to be x=0). In this case, we would not be able to differentiate between samples located at  $\pm B_0$ , resulting in aliasing about x=0 (i.e., the center of the image). We can avoid this issue by limiting the sample to either positive or negative values of x, but at the cost of losing half the sample volume. Alternatively, we can create a monotonically-varying field  $B_0(x)$  that has the same sign throughout the sample. Here we use two controllable DC power supplies to create such a gradient field by generating different currents through the coils. The resulting field strength can be estimated as follows:

$$B_0(x) = \frac{1}{2} \frac{\mu_0 N I_1 R^2}{\left(R^2 + \left(R/2 - x\right)^2\right)^{3/2}} + \frac{1}{2} \frac{\mu_0 N I_2 R^2}{\left(R^2 + \left(R/2 + x\right)^2\right)^{3/2}}, \tag{9}$$

where  $I_1$  and  $I_2$  are the currents generated by the two power supplies. Fig. 9(b) shows the theoretical and measured  $B_0$  fields across the sample volume along the z-axis. In practice, there is slight variance across the detection range because of finite sample volume. However, the influence is insignificant since the sample volume is relatively small compared to the size of the Helmholtz coils [37].

The setup described above was placed in a temperature-controlled oven to reduce fluctuations in the ambient temperature. The matching network was then connected to a commercial desktop MR spectrometer (Kea 2, Magritek) for pulse sequence generation and data acquisition. The SLSE pulse length  $t_p$  and echo spacing  $t_E$  were fixed at 50  $\mu$ s and 600  $\mu$ s, respectively to eliminate the observed dependence of  $T_{2.SLSE}$  on  $B_1$  and  $t_E$ . The resulting  $B_1$  amplitude was  $\sim 16.0$  G; this is large enough to ensure that most of the powder pattern is excited at each point in the sample (maximum length = 40 mm), which minimizes image distortion. The

resulting peak RF power level was  ${\sim}16$  W, and the data points were averaged over 64 scans.

#### 3.2. Characterization of the NaClO<sub>3</sub>-based localization system

Fig. 10 summarizes the measured values of  $T_1$  and  $T_{2.SLSE}$  versus temperature for NaClO<sub>3</sub> powder at different values of static field strength  $B_0$ . The figure shows that  $T_1$  decreases linearly with temperature, while  $T_{2.SLSE}$  remains almost constant; moreover, the NQR resonance frequency is also strongly temperature-dependent (not shown). The change of  $T_1$  with temperature is ascribed to random modulation of the EFG at the locations of resonant nuclei due to the temperature-dependent rotation of neighboring chlorate ions about their axis of threefold symmetry [36]. However,  $T_1$  does not have an obvious dependence on  $B_0$  field strength. On the other hand, the Zeeman splitting mechanism described in Section 2.3 significantly alters the value of  $T_{2.SLSE}$  with  $B_0$ , but not with temperature. As a result, the proposed relaxation-based spatial encoding mechanism is relatively robust to temperature fluctuations.

In addition to temperature, the angular dependence of  $T_{2.SISE}$  relaxation is also of interest for imaging experiments. In general, it is desirable for  $B_1$  to be set parallel to  $B_0$  (as in the previous experiments) to prevent additional powder broadening of the spectrum [38]. However, even significant deviations in the field direction from a parallel orientation merely result in decreased signal intensity. As a result, the uncertainties in determining the asymmetry parameter  $\eta$  do not greatly increase [39]. More importantly, the relaxation behavior is also relatively unaffected by  $\phi$ , which is defined as the angle between  $B_0$  and  $B_1$ . Fig. 11 shows measured values of  $T_{2.SISE}$  for NaClO<sub>3</sub> powder as a function of  $B_0$  and  $\phi$  using the SLSE sequence. No statistically significant  $\phi$ -dependence is observed, unlike for  $T_{2.SE}$  in single crystals [22].

These results verify that relaxation-based spatial encoding and imaging of NaClO<sub>3</sub> powder using different static magnetic fields is robust to both temperature fluctuations and sample orientation. Hence it is expected to be a stable and experimentally repeatable technique in practical applications.

#### 3.3. Imaging results

Time-domain data in gradient fields was collected using a SLSE pulse sequence and first converted to a  $T_{2,SLSE}$  distribution via the regularized inverse Laplace transform (ILT). The distribution was then referenced to calibrated relationships between (i) the strength of the uniform field and  $T_{2,SLSE}$  (Fig. 10); and (ii) the distribution of the gradient field across the sample (Fig. 9). Using these

relationships, the measured  $T_{2.SLSE}$  distribution can be converted to sample location, resulting in a 1D spin-density NQR image I(x). Fig. 12 shows two examples in which two slices of sodium chlorate in a tube are successfully localized using the proposed technique.

Note that the nonlinear nature of the ILT does degrade spatial resolution compared to linear methods such as the fast Fourier transform (FFT). Fig. 12 shows that the output of an ILT varies significantly for different values of SNR but the same  $\alpha$ . Therefore, sources of uncertainty in the experiments need to be reduced to a minimum. The sensitivity of the ILT to noise is of particular interest because it determines how reliable  $f(T_{2.SLSE})$  is for characterizing the spatial information within a given sample. In order to obtain a more straightforward understanding, we simplified the model to investigate the significance of noise. A singleexponential decay model  $s(t) = A \exp(-t/T_{2.SLSE})$  is simulated, where A = 0.1 and  $T_{2,SLSE} = 10$  ms. Different levels of white noise are then added to the simulated decay curve. Furthermore,  $T_{2.SLSE}$ distributions are acquired using the ILT with optimized  $\alpha$  values. Two variables are worth investigating for the  $T_{2.SLSE}$  distribution: (i) the half-width of the peak, which characterizes the precision of the distribution: the narrower the peak is, more precisely can the sample can be localized; and (ii) the log mean value of  $T_{2.SLSE}$ . The reason we use log-mean is that projections usually exhibit multiple relaxation factors and thus do not have symmetric distribution functions. As a result, their mean values on a linear scale are not good estimates for the average. Fig. 13 shows the simulated SNR versus (i) half-width of the peak, and (ii) log mean  $T_{2.SLSE}$ . Each simulation result is averaged 100 times and the optimum  $\alpha$  is selected. As SNR improves, both the peak width and variance gradually decrease, thus improving the spatial resolution. The log mean of  $T_{2.SLSE}$  is more robust to changes in SNR. In particular, it is more accurate than peak width when the SNR is relatively low.

# 3.4. Extrinsic barcode system

The approach discussed in the last section is suitable for identifying a few ILT peaks. However, when detecting complicated tagging patterns that have more than two peaks, the outputs might be difficult to differentiate using traditional analysis methods (e.g., peak-finding algorithms). Step (3) in Fig. 14 shows an example output distribution that is the combination of three exponential decay curves. The result is distorted, i.e., the peak locations don't match the actual decay constants very well, which results in a distorted image. This problem is due to the nonlinearity of the ILT and insufficient SNR of the measurements. Fortunately, machine learning classifiers can often correctly identify different

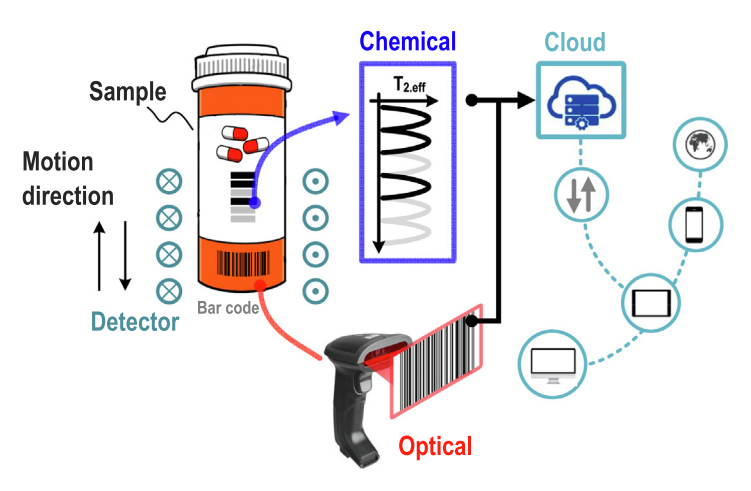


Fig. 7. Proposed approach for using "NQR barcodes" for authenticating medicines and dietary supplements.

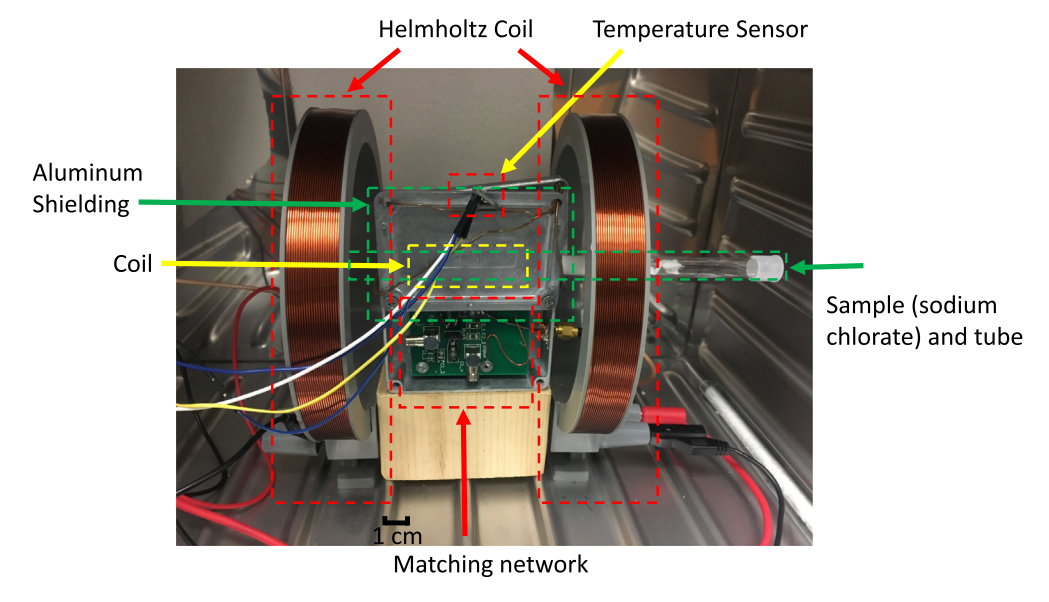
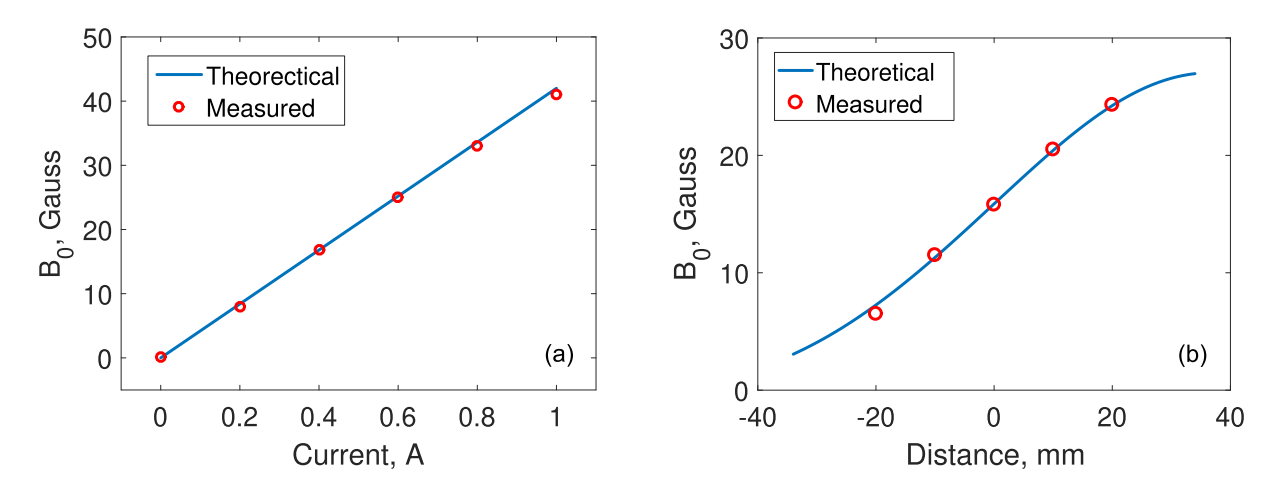
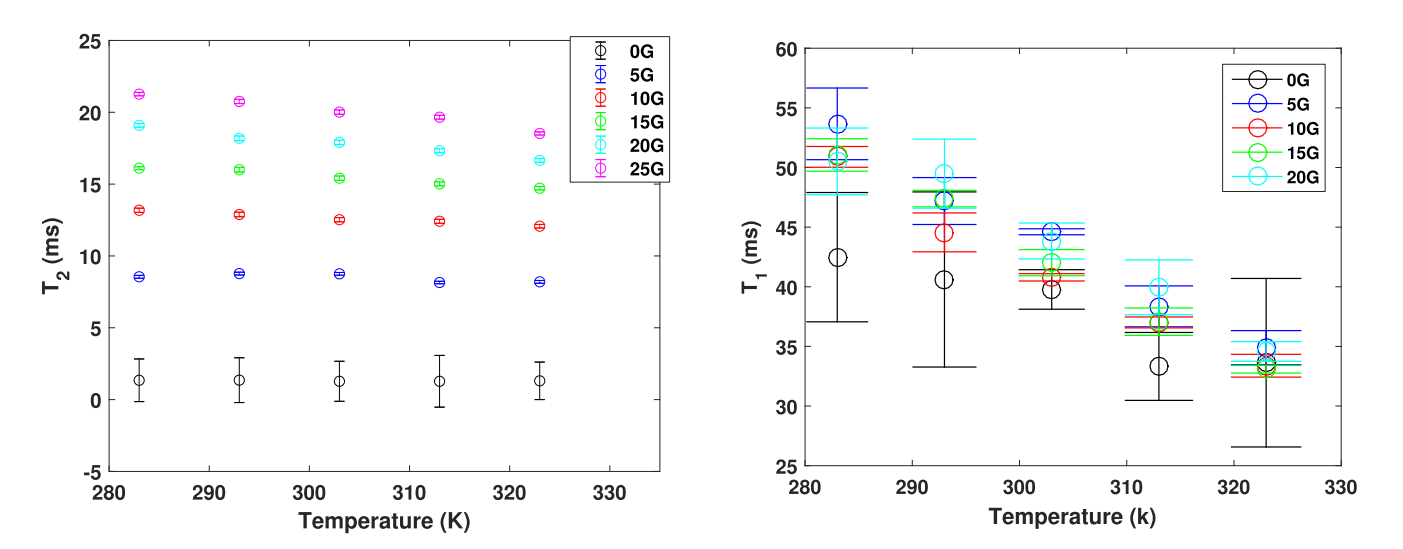


Fig. 8. Experimental setup for spatially-resolved NQR. A pair of Helmholtz-like coils is used to create a static field B<sub>0</sub> that is parallel to B<sub>1</sub> by default.



**Fig. 9.** Comparison between theoretically-estimated and measured static fields in the probe: (a) uniform  $B_0$  field generated by the Helmholtz coils, and (b) gradient  $B_0$  field used for one-dimensional spatially-localized NQR experiments. Currents used for two coils are -0.25 and 1 A respectively.



 $\textbf{Fig. 10.} \ \ \text{Left: Measured relationship between } T_{2.SLSE} \ \ \text{and temperature. Right: Measured relationship between } T_1 \ \ \text{and temperature. All data was measured from NaClO}_3 \ \ \text{powder.}$ 

ILT patterns that are visually indistinguishable. Fig. 14 shows an overview of a machine learning-based algorithm for increasing the number of unique patterns that can be distinguished, i.e., the value of  $M_1$ . It should be noted that such classification can also be performed on the raw time-domain data. However, the ILT acts as a useful data normalization, compression, and feature extraction step. We thus prefer to invert the data matrices and then perform classification on the resulting probability distributions, which provide more physical insight, lower computational complexity, and higher classification accuracy.

The proposed classification algorithm operates as follows. First we establish a suitable model and a range of possible system parameters. In the example described here, the detection area is segmented into six regions ( $b_i$ , i= 0~5), each of which can either contain the tag ('1') or not ('0'). As a result,  $M_1 = 6$  bits, and there are  $2^{M_1} = 64$  unique ILT patterns. We encode spatial information within the values of  $T_{2.SLSE}$  with the help of a gradient magnetic field and collect the time-domain data with SLSE sequence, as

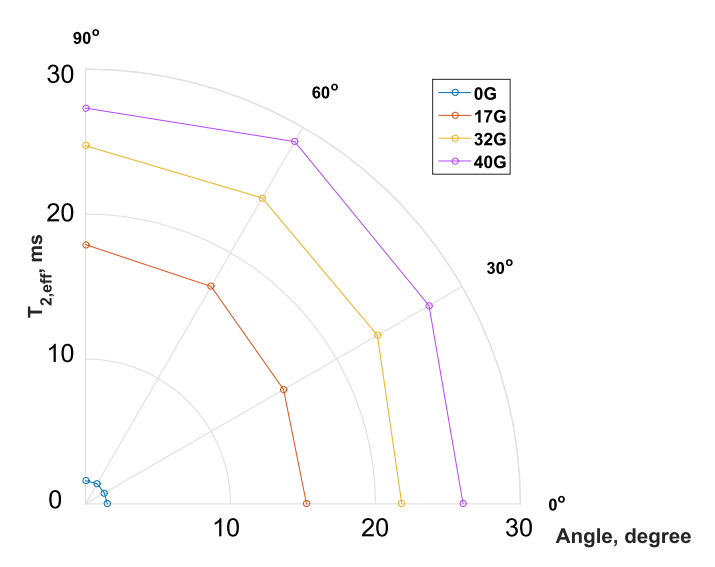


**Fig. 11.** Measured values of  $T_{2,SLSE}$  in NaClO<sub>3</sub> powder as a function of  $B_0$  and also the angle  $\phi$  between  $B_0$  and  $B_1$ . Each point is averaged 128 times. The variance of each point is around 0.2 ms.

before. We then create an array that consists of the ILT outputs regularized with different values of  $\alpha$ . Normally, the optimum value of  $\alpha$  is the best solution, but other  $\alpha$  values provide (i) robustness to changes in SNR, and (ii) some insight into the characteristics of the distributions. For example, when  $\alpha$  is closer to zero, the distribution tends to be less smooth and converges to a specific value. Note that this value is not necessarily equal to the true value of  $T_{2.SLSE}$  due to the numerically ill-posed nature of the ILT in the presence of noise. As an example, Fig. 15 shows ILT results after regularization with different  $\alpha$  values for SLSE data with typical SNR.

Furthermore, the trend of how the distribution converges provides another dimension of information. Specifically, in our case, we train the algorithm on distributions generated by the following values of  $\alpha$ : (i) the optimum value obtained from the BRD method, and (ii)  $10^{-x}$ , where x represents an integer from 1 to 6. The chosen machine learning algorithm is trained off-line to recognize a set of ILT patterns. Prediction accuracy is then evaluated using cross validation. For each pattern, at least 100 sets of data are collected, where each set has 7000 features: 1,000 1000 points per  $T_{2.SLSE}$  distribution, times 7 distributions (one for each value of  $\alpha$ ). After classification, if the mean value of the distribution within a region of T<sub>2.SLSE</sub> space exceeds a threshold value, we consider the corresponding bit to be a '1'; otherwise, it is a '0'. Here, the regions for calculating means are carefully chosen based on simulation such that they can be reliably distinguished from each other after the ILT. The values chosen for these ranges also ensure that the tagging pattern is still identifiable when there are slightly offsets in the gradient field. In the simulated experiment, the mean values of the ranges are defined as 1, 5, 10, 15, 20, and 25 ms. Note that the relationship between the  $B_0$  field and  $T_{2.SISE}$  is non-linear, so if more bits is required in the future, a non-uniform value assignment is desired to ensure that the barcode system does not get easily corrupted. In addition, while we just trained the algorithm on 20 different 3-peak and 4-peak patterns for demonstration purposes, the approach can be extended to all possible  $M_1$ -bit patterns (in this example,  $M_1 = 6$ ).

A generalized version of the proposed authentication procedure can be briefly summarized as follows:

- 1. Segment the detection space  $b_i$ .
- 2. Encode spatial information within the values of  $T_{2.SLSE}$  and collect time-domain data with the SLSE sequence.

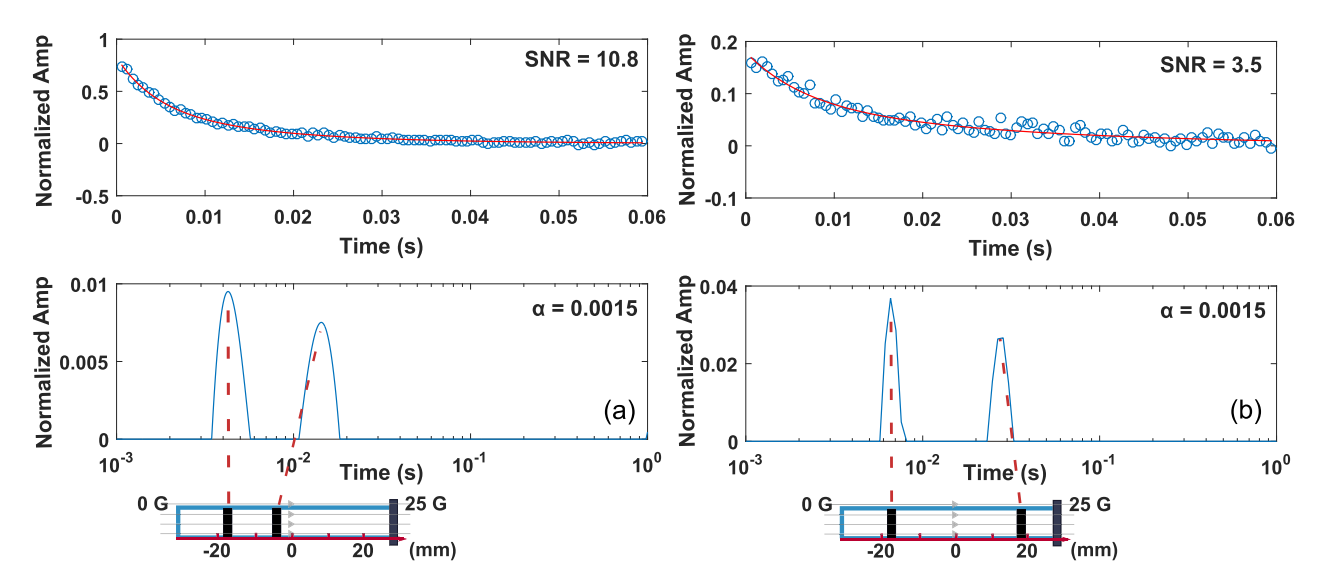
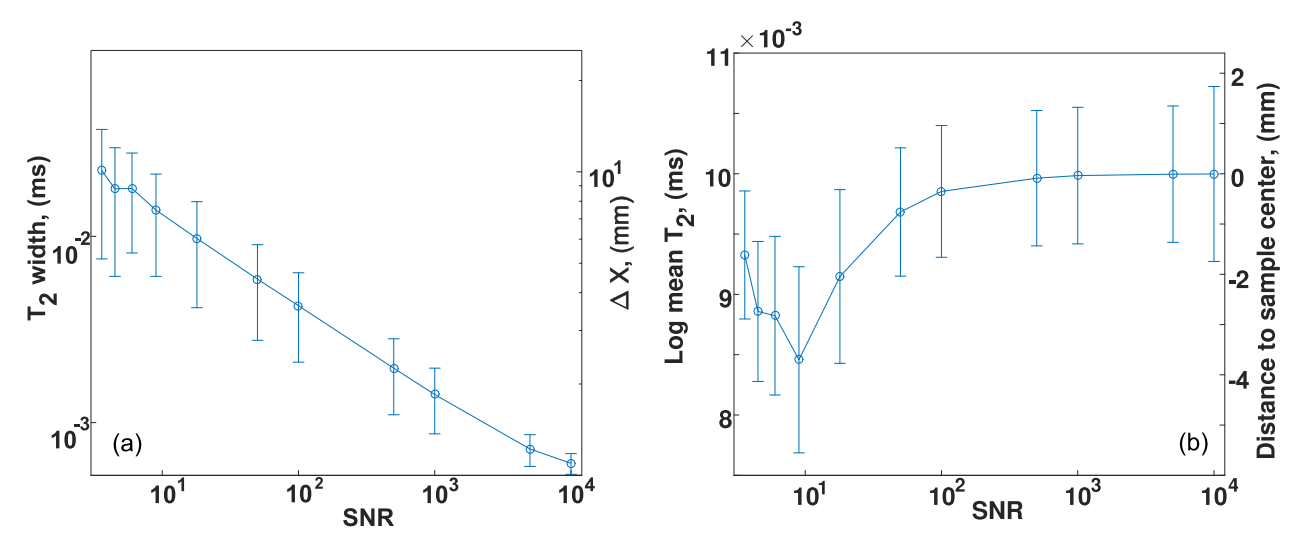


Fig. 12. Measured data from a sample consisting of two slices of sodium chlorate: (a) placed close to each other (separation  $\approx 18\,$  mm), (b) placed far away from each other (separation  $\approx 36\,$  mm). Each slice has a diameter of 10 mm and is about 1 cm long, resulting in a mass of  $\sim 2.5\,$  gm.



**Fig. 13.** Noise analysis of a mono-exponential relaxation decay  $s(t) = A \exp(-t/T_{2,SLSE})$ , where  $T_{2,SLSE} = 10$  ms and amplitude A = 0.1. (a) Half-width of  $T_{2,SLSE}$  peak with different SNR. (b) Log mean of  $T_{2,SLSE}$  with different SNR.

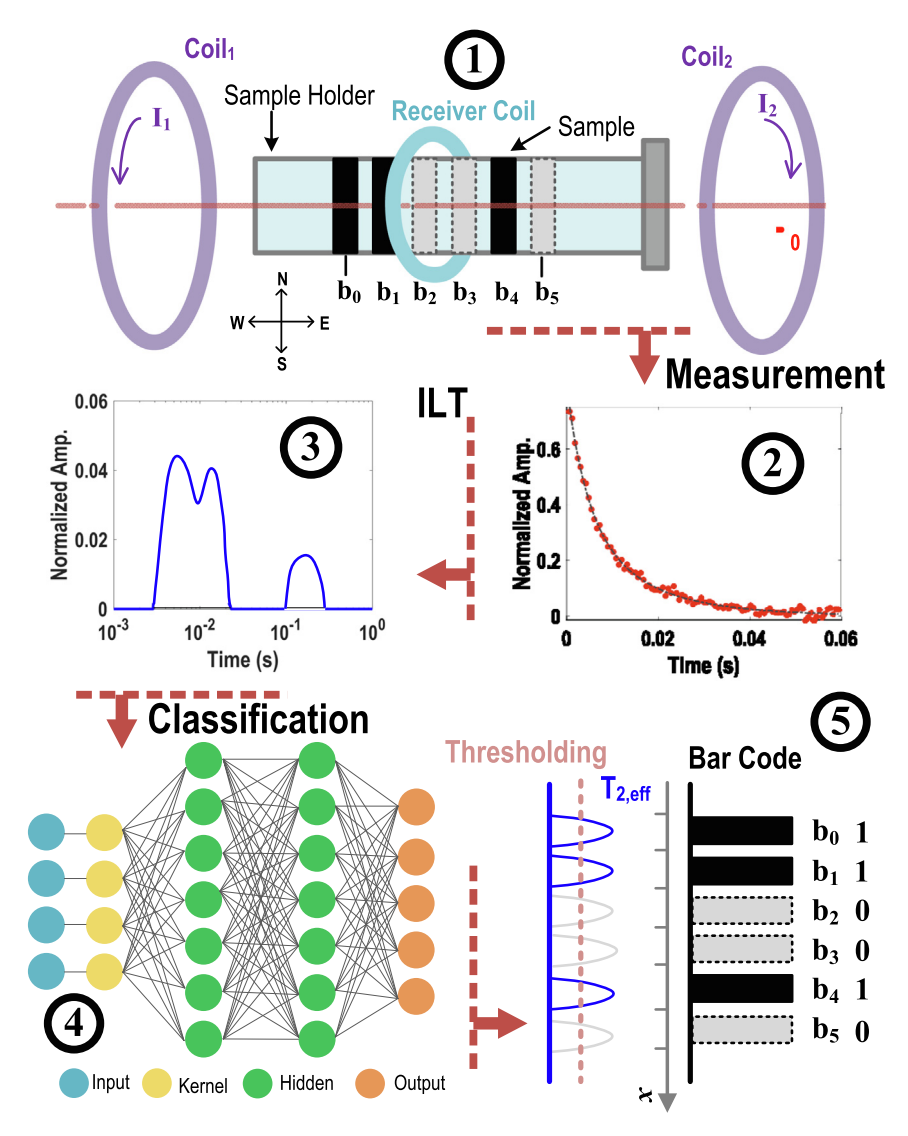


Fig. 14. Flowchart of the proposed NQR-based "barcode" approach for authenticating objects.

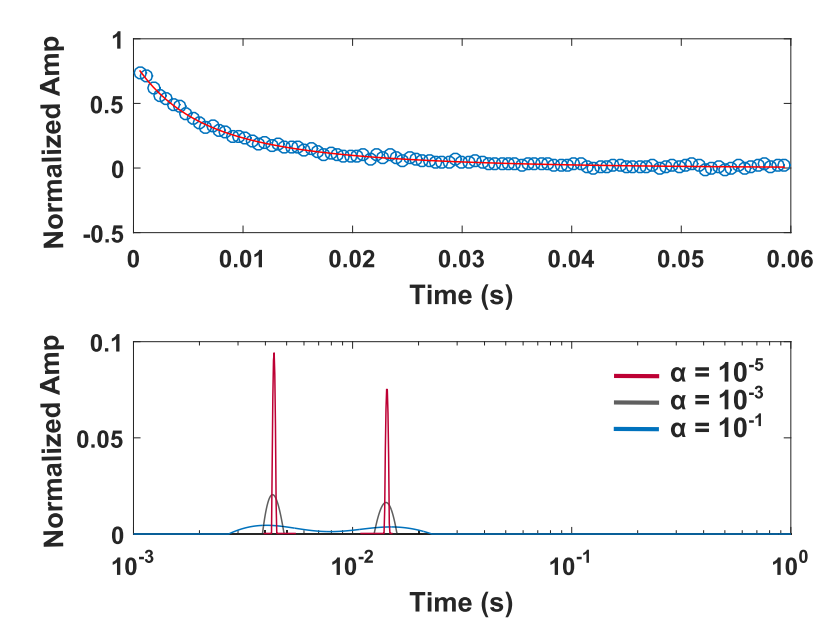
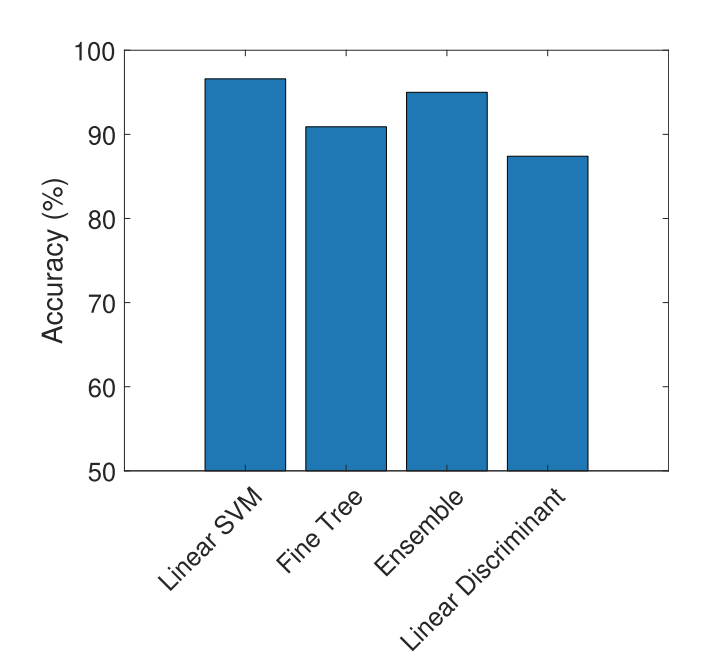


Fig. 15. ILT results after regularization with different  $\alpha$  values for SLSE data with typical SNR.



**Fig. 16.** Prediction accuracy for a subset of classification algorithms tested on barcode patterns obtained from simulated SLSE data with realistic SNR.

- 3. Generate a test array that consists of the ILT outputs regularized with different values of  $\alpha$ .
- 4. Feed the array into a trained model and identify the corresponding pattern.
- 5. Transform the pattern into spatial information and retrieve the barcode.

Fig. 16 summarizes the prediction accuracy of a subset of classification algorithms for simulated data with similar SNR as in the experiments. We also show a full summary of the results in C. Some of the algorithms have shown a prediction accuracy of above 95%. Linear SVM is the most efficient algorithm with 96.6% accuracy.

#### 3.5. Experimental verification of NQR-based barcodes

The simulation model was further verified by using customized 3D-printed prototypes, one of which is shown in Fig. 17. The parts are designed in commercial computer-aided design software (SolidWorks from Dassault Systèmes) and then fabricated on a commercial 3D printer (Xinkebot). They consist of cylinders containing multiple uniformly-spaced slots that can be filled with an NQR-active compound in powder form. Therefore, each slot is able to encode one-bit information: the ones filled with powder encode '1', while the rest encode '0'. This procedure effectively turns the



**Fig. 17.** A 3D-printed model of an NQR-tagged object with 32 slots. Each slot is about 4 mm wide. The gap between slots is about 3 mm. Some of the slots are selectively filled with pure sodium chlorate powder and can be considered as '1' bits; the rest are '0' bits. After filling, the slots are sealed with Parafilm to block moisture. Each slot can contain about 0.8 gm of the sample.

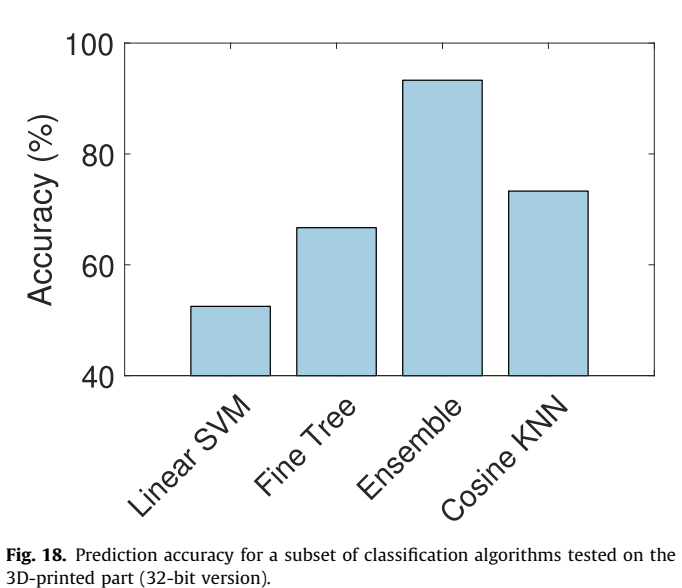


Fig. 18. Prediction accuracy for a subset of classification algorithms tested on the 3D-printed part (32-bit version).

prototype into an "embedded barcode" system as described above. Furthermore, the prototype is carefully designed so that it fits within the setup mentioned in Section 3.1. At the moment, pure sodium chlorate powder is used to fill the slots in order to obtain good SNR. Eventually the parts can be redesigned to be directly printed out on a dual-filament printer in which one filament contains a small fraction of the NQR-active compound. In this way, the printed structure would be convenient for NOR detection while ensuring that the tags are difficult to detect, which would in turn increase the difficulty of counterfeiting and thus the security of NOR-based authentication.

We followed the proposed approach as described above by filling a random subset of slots on the 32-bit prototype. Then the part was fed inside the coil and scanned through. Note that the detection area for the coil can only contain six slots (6 bits) for a single scan. Therefore, in order to complete the analysis of entire encoded information in the prototype, at least six scans have to be conducted. Fig. 18 shows the prediction accuracy for the scanning results. The prediction accuracy drops compared to the simulation results. There are several possible reasons for the degradation, including: (i) The gradient magnetic field is not linear enough, thus causing spatial distortion artifacts due to errors in the encoding relaxation rates. (ii) The finite width of each slot results in a

multi-exponential decay curve for the sample within that slot. (iii) There is some variation between the amounts of sample contained in each slot due to the manual filling procedure. This results in variable SNR for different slots, which in turn creates classification errors by distorting the inverted distributions.

In spite of these experimental challenges, the "ensemble" classifier available in MATLAB, which attempts to meld results from many weak learners into one high-quality ensemble predictor, provides good classification accuracy of 93.3%. As a result, the embedded barcode can be read with 100% accuracy by adding a small number of extra bits for digital error-correction. In addition, the raw error rate can be reduced by using a dual-filament 3D printer to manufacture tagged parts with high repeatability, as described earlier.

### 3.6. Other chlorine compounds

In Fig. 19, we show that the  $T_{2.SLSE}$  values of two other chlorine compounds (hydrochlorothiazide and furosemide) also increase with  $B_0$ , although not as strongly as for sodium chlorate. In NaClO<sub>3</sub>, each chlorine nucleus is located at the apex of a chlorate anion (which has a trigonal pyramidal structure), and its ionic bond with the nearest sodium nucleus is aligned with the axis of this pyramid. As a result, the local EFG tensor is axisymmetric, with a low value for the asymmetry parameter  $\eta$ . By contrast, the chlorine nuclei in hydrochlorothiazide and furosemide are covalently bound to a benzene ring, as shown in Fig. 19. Such molecular structures are non-planar and have low symmetry, which results in larger values of  $\eta$  for the local EFG tensor. Earlier work on Zeeman-perturbed NOR has shown that there is less Zeeman splitting (i.e., a narrower powder pattern) as  $\eta$  increases [40]. Thus, we expect a less significant increase of  $T_{2 \text{ SISE}}$  with  $B_0$  for nuclear sites with higher  $\eta$ , in agreement with our experimental results. The weaker field-dependence of  $T_{2.SLSE}$  also leads to degraded spatial resolution. As a result, we limited our imaging experiments and simulations to NaClO<sub>3</sub>. Nevertheless, the results in Fig. 19 indicate that the proposed technique is applicable to other chlorine compounds as well.

#### 4. Summary and conclusions

We have presented a relaxation-based approach to spatiallyresolved NQR. The feasibility of the approach has been proven both theoretically and experimentally. Existing results on field-

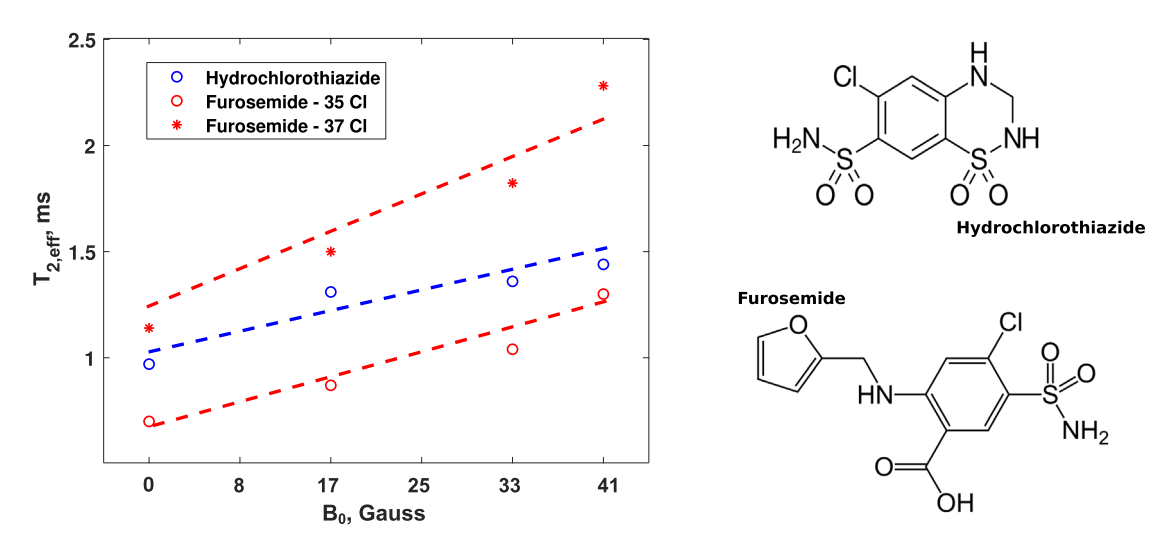


Fig. 19. Measured  $T_{2.835}$  values of hydrochlorothiazide (blue) and furosemide (red) as a function of field strength  $B_0$ . (For interpretation of the references to color in this figure legend, the reader is referred to the web version of this article.)

dependent SE relaxation of single-crystal sodium chlorate have been extended to SLSE relaxation of powder samples. The results have been used to improve the security of NQR-based authentication tags by enabling single-shot readout of spatially-resolved tagging patterns ("NQR barcodes"). The spatial resolution of relaxation-based imaging is limited by the nonlinear nature of the ILT, so the proposed method is only capable of extracting spatial features rather than generating true images. However, the use of a machine learning algorithm can significantly improve the effective resolution, making our approach promising for various authentication applications.

The proposed authentication method can be improved in several ways. The first is "grey scale" encoding, in which each spatial region of the barcode can store multiple bits to further improve security. However, the quantity of sodium chlorate tag in each region needs to be carefully controlled in order to realize such a grey scale code, which presents fabrication challenges. The second is an automated motion control system for the detection coil (i.e., probe) to eliminate the need for manual scanning. The third is closed-loop temperature compensation. While the SLSE relaxation rates are relatively temperature-insensitive, the resonant frequencies are not. As a result, it is desirable for long experiments to include continuous tracking of the sample temperature such that the resulting shifts in resonant frequency can be automatically compensated.

# Acknowledgements

The authors would like to acknowledge the National Science Foundation (NSF) for funding support. This work was partially funded by the NSF through grant CCF-1563688.

#### Appendix A. Estimation of average echo amplitudes

The amplitude of the average echo shape (without noise) obtained by adding up a series of  $N_E$  echoes generated by an SLSE sequence can be written as follows:

$$s_{tot} = s(0) \sum_{k=1}^{N_E} e^{-kt_E/T_{2,SLSE}} = s(0) \frac{1 - e^{-N_E t_E/T_{2,SLSE}}}{1 - e^{-t_E/T_{2,SLSE}}}. \tag{A.1} \label{eq:stot}$$

It is generally safe to assume that  $t_E \ll T_{2.SLSE}$ . In this case  $1 - e^{-t_E/T_{2.SLSE}} \approx 1 - 1 + t_F/T_{2.SLSE} = t_F/T_{2.SLSE}$ , so we get

$$s_{tot} = s(0) \left( \frac{T_{2,SLSE}}{t_E} \right) \left( 1 - e^{-N_E t_E / T_{2,SLSE}} \right).$$
 (A.2)

Note that matched filtering can be used to maximize SNR; in this case each received echo is weighted by its expected SNR before summation [41]. For the k-th echo, the additional weighting factor is  $e^{-kt_E/T_2}$  since the signal decays exponentially while the noise remains constant. If used, it is desired that the influence of this weighting factor is removed as well. It is easy to do this by modifying Eqn. (A.1).

Similarly, for a SE sequence, the average echo shape (obtained by adding up echoes from  $N_E$  scans with linearly-increasing values of  $t_E$ ) is given by

$$s_{tot} = s(0) \sum_{k=1}^{N_E} e^{\frac{-k^2 t_E^2}{2T_{2.SE}^2}}.$$
 (A.3)

There is no closed-form expression for this result, but it is easy to evaluate numerically.

# Appendix B. Summary of machine learning algorithm

Recent advancements in machine learning suggest its importance in interpreting and classifying complex datasets for decision analysis. In particular, machine learning algorithms are effective for authentication and discrimination of food items and pharmaceutical products [42,20]. Here we utilized the MATLAB Classification Learner application (Mathworks, Natick, MA) to test a variety of modern machine learning algorithms on  $f(T_{2.SLSE})$  distributions generated by Laplace inversion of SLSE data. We then used 10-fold validation to test the accuracy of each algorithm. We focus on four different categories of algorithms: decision trees, discriminants, support vector machines (SVMs), and k-nearest neighbors (KNNs). These methods are briefly introduced below. A more detailed description is available in [43].

Decision trees uses tree-like models of decisions and their possible consequences. It classifies instances by sorting them down the tree by branches based on attribute values tests. Decision trees are often used because they are easily comprehensible.

Discriminant analysis methods find a set of prediction equations based on independent variables. It reduce dimensionality by selecting data labels that maximize the separation between training sets. They can be good candidates to address supervised learning problems where the goals are to find the directions along which the data is best separable.

*SVMs* try to separate the data into classes by drawing a hyperplane between training set categories. These algorithms build models such that each instance behaves as a non-probabilistic bin-

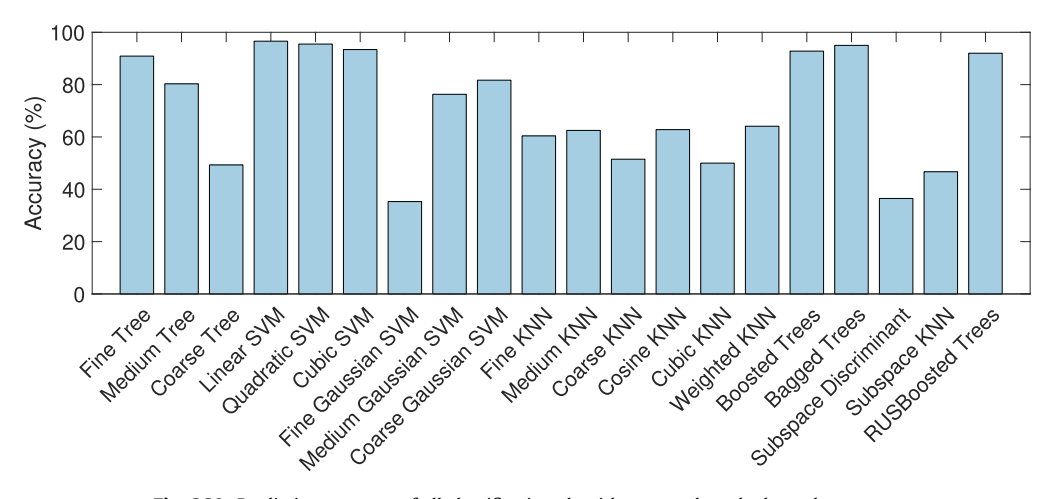


Fig. C.20. Prediction accuracy of all classification algorithms tested on the barcode patterns.

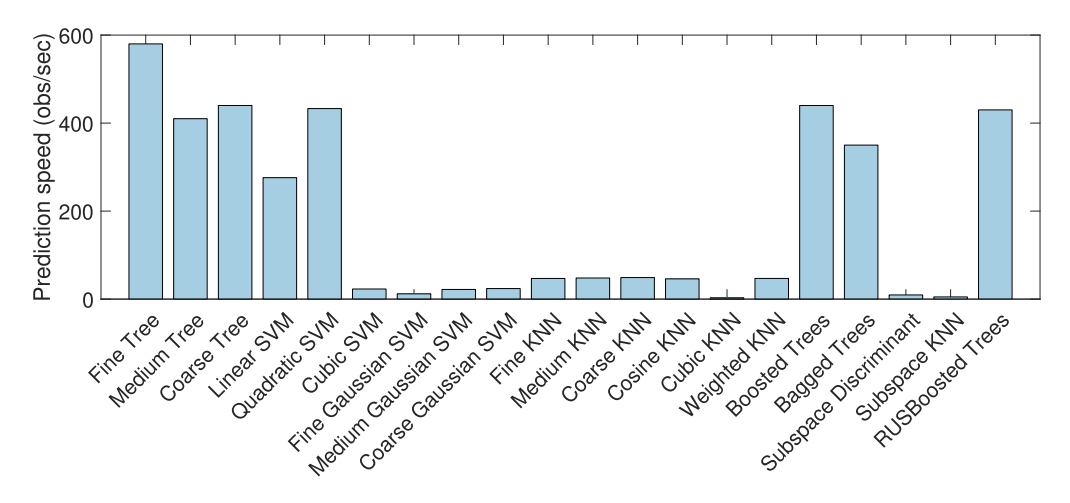


Fig. C.21. Prediction speed of all classification algorithms tested on the barcode patterns.

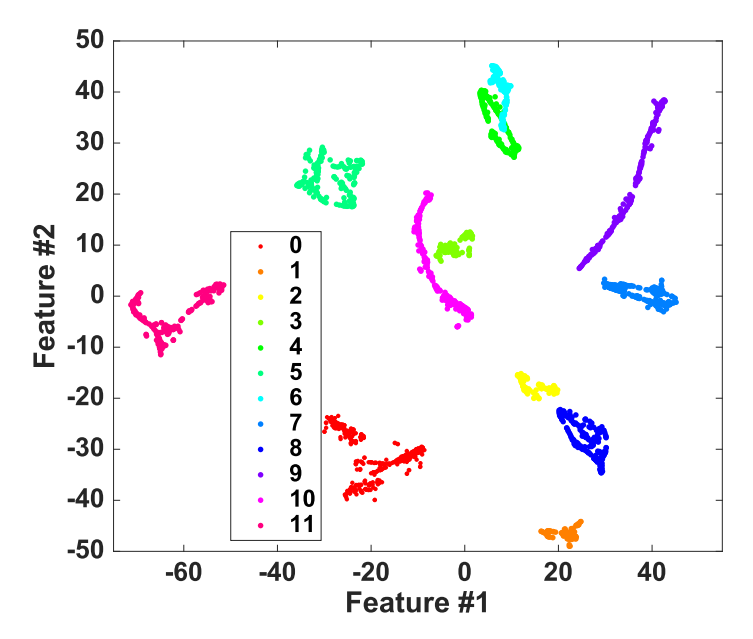


Fig. C.22. An example of selected features used for mapping of different barcode patterns.

ary linear classifier. Multiple SVM instances can be combined together to handle any number of classes.

KNNs are non-parametric methods that rely on the assumption that data classified with the same label will have features that lie near each other when plotted. They are simple but lazy learning algorithms with relatively high computational costs.

#### Appendix C. Summary of classification data

For completeness, this appendix summarizes classification results obtained using all 20 algorithms available in the MATLAB Classification Learner application. Figs. C.20 and C.21 respectively summarize prediction accuracy and prediction speed for the peak patterns.

Fig. C.22 shows an example of visualizing a high-dimensional feature map for different ILT patterns using t-Distributed Stochastic Neighbor Embedding (t-SNE). In the map, the majority of the features are well separated, resulting in high classification accuracy. There are 7000 features in total.

#### References

- [1] Z. Lavric, J. Pirnat, J. Luznik, J. Seliger, V. Zagar, Z. Trontelj, S. Srcic, Application of 14N NQR to the study of piroxicam polymorphism, J. Pharm. Sci. 99 (12) (2010) 4857–4865.
- [2] E. Tate, K. Althoefer, J. Barras, M.D. Rowe, J.A. Smith, G.E. Pearce, S.A. Wren, Quantitative 35Cl nuclear quadrupole resonance in tablets of the antidiabetic medicine diabinese, Anal. Chem. 81 (13) (2009) 5574–5576.
- [3] J. Fraissard, O. Lapina, Explosives Detection Using Magnetic and Nuclear Resonance Techniques, Springer Science & Business Media, 2009.
- [4] J.B. Miller, Nuclear quadrupole resonance detection of explosives, in: Counterterrorist Detection Techniques of Explosives, Elsevier, 2007, pp. 157–198.
- [5] J. Barras, D. Murnane, K. Althoefer, S. Assi, M.D. Rowe, I.J. Poplett, G. Kyriakidou, J.A. Smith, Nitrogen-14 nuclear quadrupole resonance spectroscopy: a promising analytical methodology for medicines authentication and counterfeit antimalarial analysis, Anal. Chem. 85 (5) (2013) 2746–2753.
- [6] C. Chen, F. Zhang, J. Barras, K. Althoefer, S. Bhunia, S. Mandal, Authentication of medicines using nuclear quadrupole resonance spectroscopy, IEEE/ACM Trans. Comput. Biol. Bioinformatics 13 (3) (2015) 417–430.
- [7] V. Mikhaltsevitch, T. Rudakov, J. Flexman, P. Hayes, W. Chisholm, Multipulse sequences for explosives detection by nqr under conditions of magnetoacoustic and piezoelectric ringing, Appl. Magn. Reson. 25 (3-4) (2004) 449.

- [8] L. Cardona, Y. Miyato, H. Itozaki, J. Jiménez, N. Vanegas, H. Sato-Akaba, Remote detection of ammonium nitrate by nuclear quadrupole resonance using a portable system, Appl. Magn. Reson. 46 (3) (2015) 295–307.
- [9] W. Shao, J. Barras, P. Kosmas, Detection of extremely weak NQR signals using stochastic resonance and neural network theories, Signal Process. 142 (2018) 96–103
- [10] J. Lužnik, J. Pirnat, V. JazbinŠek, Z. Trontelj, T. Apih, A. GregoroviČ, R. Blinc, J. Seliger, Polarization enhanced NQR detection at low frequencies, in: Explosives Detection Using Magnetic and Nuclear Resonance Techniques, Springer, 2009, pp. 41–56.
- [11] J. Glickstein, S. Mandal, An automated instrument for polarization-enhanced broadband nuclear quadrupole resonance (NQR) spectroscopy, Rev. Sci. Instrum. 89 (9) (2018) 093106.
- [12] B. Venhuis, M. Zwaagstra, P. Keizers, D. De Kaste, Dose-to-dose variations with single packages of counterfeit medicines and adulterated dietary supplements as a potential source of false negatives and inaccurate health risk assessments, J. Pharm. Biomed. Anal. 89 (2014) 158–165.
- [13] J. Barras, S. Katsura, H. Sato-Akaba, H. Itozaki, G. Kyriakidou, M.D. Rowe, K.A. Althoefer, J.A. Smith, Variable-pitch rectangular cross-section radiofrequency coils for the nitrogen-14 nuclear quadrupole resonance investigation of sealed medicines packets, Anal. Chem. 84 (21) (2012) 8970–8972.
- [14] S. Matsui, K. Kose, T. Inouye, An NQR imaging experiment on a disordered solid, J. Magn. Reson. (1969) 88 (1) (1990) 186–191.
- [15] E. Rommel, R. Kimmich, H. Robert, D. Pusiol, A reconstruction algorithm for rotating frame NQR imaging ( $\rho$ NQRI) of solids with powder geometry, Meas. Sci. Technol. 3 (5) (1992) 446.
- [16] E. Rommel, P. Nickel, R. Kimmich, D. Pusiol, Rotating-frame NQR imaging, J. Magn. Reson. (1969) 91 (3) (1991) 630–636.
- [17] S. Aissani, L. Guendouz, P.-L. Marande, D. Canet, Toward nitrogen-14 nuclear quadrupole resonance imaging by nutation experiments performed with a radio-frequency field gradient, Solid state Nucl. Magn. Reson. 84 (2017) 41–44.
- [18] T. Rudberg, A. Jakobsson, Robust detection of nuclear quadrupole resonance signals in a non-shielded environment, in: 2011 19th European Signal Processing Conference, IEEE, 2011, pp. 2079–2083.
- [19] J. Lehmann-Horn, D. Miljak, L. O'Dell, R. Yong, T. Bastow, Rapid detection of arsenic minerals using portable broadband nqr, Geophys. Res. Lett. 41 (19) (2014) 6765–6771.
- [20] N.V.R. Masna, C. Chen, S. Mandal, S. Bhunia, Robust authentication of consumables with extrinsic tags and chemical fingerprinting, IEEE Access 7 (2019) 14396–14409.
- [21] B.H. Suits, Nuclear quadrupole resonance spectroscopy, in: Handbook of Applied Solid State Spectroscopy, Springer, 2006, pp. 65–96.
- [22] E. Hahn, B. Herzog, Anisotropic relaxation of quadrupole spin echoes, Phys. Rev. 93 (3) (1954) 639.
- [23] M. Bloom, E. Hahn, B. Herzog, Free magnetic induction in nuclear quadrupole resonance, Phys. Rev. 97 (6) (1955) 1699.
- [24] M. Bloom, "Slow beats" in nuclear quadrupole induction, Phys. Rev. 94 (5) (1954) 1396.

- [25] N. Ainbinder, G. Furman, G. Kibrik, A.Y. Poljakov, I. Shaposhnikov, Relaxation processes in NQR multiple-pulse spin-locking, Zeitschrift für Naturforschung A 41 (1–2) (1986) 366–369.
- [26] J. Keeler, Understanding NMR Spectroscopy, John Wiley & Sons, 2011.
- [27] J. Van Vleck, The dipolar broadening of magnetic resonance lines in crystals, Phys. Rev. 74 (9) (1948) 1168.
- [28] M.M. Maricq, Quasistationary state and its decay to equilibrium in the pulsed spin locking of a nuclear quadrupole resonance, Phys. Rev. B 33 (7) (1986) 4501.
- [29] R. Ramachandran, P. Narasimhan, Zeeman perturbed nuclear quadrupole spin echo envelope modulations for spin 3/2 nuclei in polycrystalline specimens, Mol. Phys. 48 (2) (1983) 267–282.
- [30] Y.-Q. Song, L. Venkataramanan, M. Hürlimann, M. Flaum, P. Frulla, C. Straley, T1–T2 correlation spectra obtained using a fast two-dimensional laplace inversion, J. Magn. Reson. 154 (2) (2002) 261–268.
- [31] J. Butler, J. Reeds, S. Dawson, Estimating solutions of first kind integral equations with nonnegative constraints and optimal smoothing, SIAM J. Numer. Anal. 18 (3) (1981) 381–397.
- [32] S. Kovacs, S.E. Hawes, S.N. Maley, E. Mosites, L. Wong, A. Stergachis, Technologies for detecting falsified and substandard drugs in low and middle-income countries, PloS One 9 (3) (2014) e90601.
- [33] J. Lužnik, J. Pirnat, Z. Trontelj, Measurement of temperature and temperature gradient inámillimeter samples by chlorine NQR, Appl. Phys. A 96 (4) (2009) 1023–1026.
- [34] K. Ramesh, K. Suresh, C. Raghavendra Rao, J. Ramakrishna, Pressure and temperature dependence of the chlorine NQR in caesium and sodium chlorates, Magn. Reson. Chem. 46 (6) (2008) 525–533.
- [35] T. Krishnamoorthy, P. Babu, J. Ramakrishna, Temperature and pressure dependence of 35Cl nqr in NaClO3 and Ba(ClO3) 2·H2O, J. Mol. Struct. 249 (2–4) (1991) 377–390.
- [36] R.C. Zamar, C.E. González, D.J. Pusiol, Temperature-induced orientational disorder in NaClO3, Phys. Rev. B 58 (5) (1998) 2476.
- [37] J.C. Simpson, J.E. Lane, C.D. Immer, R.C. Youngquist, Simple analytic expressions for the magnetic field of a circular current loop.
- [38] B. Suits, G. Plude, Gradient coils and NQR imaging of powders, J. Magn. Reson. Ser. A 117 (1) (1995) 84–87.
- [39] Y. Morino, T. Chiba, T. Shimozawa, M. Toyama, Zeeman effect of nuclear quadrupole resonance spectrum in cyanuryl chloride, J. Phys. Soc. Jpn. 13 (8) (1958) 869–879.
- [40] N.S. Bai, N. Reddy, R. Ramachandran, Zeeman-perturbed spin-echo FT NQR spectroscopy, J. Magn. Reson. Ser. A 102 (2) (1993) 137–143.
- [41] C. Ropp, C. Chen, M. Greer, J. Glickstein, L. Mair, O. Hale, D. Ariando, S. Jafari, A. Hevaganinge, S. Mandal, et al., Electropermanent magnets for variable-field NMR, J. Magn. Reson. 303 (2019) 82–90.
- [42] G.P. Danezis, A.S. Tsagkaris, V. Brusic, C.A. Georgiou, Food authentication: state of the art and prospects, Curr. Opin. Food Sci. 10 (2016) 22–31.
- [43] S.B. Kotsiantis, I. Zaharakis, P. Pintelas, Supervised machine learning: a review of classification techniques, Emerg. Artif. Intell. Appl. Comput. Eng. 160 (2007) 3–24.